PAPER

Check for updates

Beyond hydrophobicity: how F4-TCNQ doping of the hole transport material improves stability of mesoporous triple-cation perovskite solar cells†

Maning Liu, [ID] [a] Staffan Dahlström,[b] Christian Ahläng,[b] Sebastian Wilken,[b] Aleksandr Degterev, [ID] [a] Anastasia Matuhina,[a] Mahboubeh Hadadian,[c] Magnus Markkanen,[d] Kerttu Aitola,[d] Aleksi Kamppinen, [ID] [e] Jan Deska, [ID] [f] Oliver Mangs,[b] Mathias Nyman,[b] Peter D. Lund,[d] Jan-Henrik Smått,[c] Ronald Österbacka*[b] and Paola Vivo [ID] *[a]

Despite the outstanding power conversion efficiency of triple-cation perovskite solar cells (PSCs), their low long-term stability in the air is still a major bottleneck for practical applications. The hygroscopic dopants traditionally used in hole transport materials (HTMs) severely degrade the perovskite film. The p-type F4-TCNQ doping of the well-known spiro-OMeTAD HTM enables hydrophobicity-induced protection of the perovskite layer underneath. Nevertheless, the mechanism of F4-TCNQ doping in stabilizing PSCs is still rather unclear. Herein, when F4-TCNQ was adopted as the sole dopant of spiro-OMeTAD, highly stable mesoporous triple-cation PSCs were developed, with a very long T_{80} lifetime of more than 1 year ($\sim$380 days) for devices stored in air (RH $\sim$ 40%). The present comprehensive experimental and theoretical studies on F4-TCNQ-doped spiro-OMeTAD reveal that the hydrophobic protection of the perovskite layer underneath is not the only reason for the increased long-term stability of the devices. The high uniformity of F4-TCNQ doping in the spiro-OMeTAD layer and less dopant aggregation and dopant migration towards the anode are key factors responsible for the increased stability of the perovskite solar cells when compared to conventional hygroscopic dopants. This work paves the way for future doping engineering of HTMs for PSCs with competitive stability.

Introduction

Over the last decade, the power conversion efficiency (PCE) of metal halide perovskite solar cells (PSCs) has rapidly exceeded 25%,[1] which is comparable to silicon solar cells. Despite the

[a]Hybrid Solar Cells, Faculty of Engineering and Natural Sciences, Tampere University, P. O. Box 541, FI-33014 Tampere, Finland. E-mail: paola.vivo@tuni.fi

[b]Physics, Faculty of Science and Engineering, Åbo Akademi University, 20500 Turku, Finland

[c]Laboratory of Molecular Science and Engineering, Faculty of Science and Engineering, Åbo Akademi University, 20500 Turku, Finland

[d]New Energy Technologies Group, Department of Applied Physics, Aalto University, School of Science, P. O. Box 15100, 00076 Aalto (Espoo), Finland

*[e]Department of Mechanical and Materials Engineering, University of Turku, 20014 Turku, Finland*

[f]Department of Chemistry and Materials Science, Aalto University, Espoo, Finland

† Electronic supplementary information (ESI) available: Experimental details, absorption spectra, stability of the champion device with no doped spiro-OMeTAD, tables that summarize the performance of the devices with different concentrations of F4-TCNQ doping and water contact angles, devices aging with maximum power point tracking, thermal stability test, storage-time dependent time-resolved photoluminescence decays, drift-diffusion simulations, stability study on the devices stored in a dry cabinet (RH < 10%). See https://doi.org/10.1039/d2ta02588d

continuous improvements in the PCE, the low stability of PSCs still hinders their commercialization. Most high-performing PSCs require highly conductive charge (electron and hole) transport layers to realize efficient charge extraction in the devices. While the conventional electron transport materials (ETMs), such as TiO_2 and [6,6]-phenyl-C61-butyric acid methyl ester (PCBM), possess intrinsically high electron conductivity, the most widely used organic hole transport materials (HTMs), *e.g.*, 2,2′,7,7′-tetrakis[*N*,*N*-di(4-methoxyphenyl)amino]-9,9′-spirobifluorene (spiro-OMeTAD) and poly[bis(4-phenyl)(2,4,6-trimethylphenyl)amine] (PTAA), normally require the addition of dopants, typically lithium bis(trifluoromethanesulfonyl) imide (LiTFSI), *tert*-butylpyridine (*t*BP), and tris(2-(1*H*-pyrazol-1-yl)-4-*tert*-butylpyridine)cobalt(III) tri[bis(trifluoromethane)sulfonimide] (FK209), to achieve high hole conductivity for top-performing devices.[2–4] However, the addition of these dopants can cause severe degradation in both the HTM and perovskite layer, leading to shortened device lifetimes.[5,6] For instance, the hygroscopic nature of LiTFSI is responsible for its moisture absorption from the environment and the LiTFSI-doped spiro-OMeTAD can induce the formation of a large number of pinholes in the layer, facilitating moisture penetration and significant degradation of the perovskite layer.[7] In addition, the

This journal is © The Royal Society of Chemistry 2022

J. Mater. Chem. A, 2022, **10**, 11721–11731 | 11721

introduction of *t*BP dopant in spiro-OMeTAD corrodes the perovskite layer *via* interfacial contact between perovskite and HTM and results in the formation of a [PbI$_2$·*t*BP] coordinated complex, further decomposing the perovskite structure.[8] Therefore, major research efforts have been devoted to identifying alternative dopants for spiro-OMeTAD or developing dopant-free alternative HTMs, tackling the achievement of both high efficiency and the stability of PSCs at the same time. Several dopants with complex molecular structures, *e.g.*, Co(PzPy)$_3$(TFSI)$_3$, Ag-TFSI, and tris(2-(1*H*-pyrazol-1-yl)pyridine) cobalt(ɪɪ) di[bis(trifluoromethane)sulfonimide] (FK102), have also been used as additives for spiro-OMeTAD to achieve highly efficient devices. However, their hydrophilic natures have led to detrimental effects on device stability.[8–10] Hence, a simple and highly conductive molecular dopant with non-hygroscopic nature is crucial to achieving highly efficient and stable PSCs.

The organic molecule 2,3,5,6-tetrafluoro-7,7,8,8 tetracyanoquinodimethane (F4-TCNQ) is a tetracyanoquinodimethane (TCNQ) derivative, possesses not only good electron-accepting capability for forming charge-transfer complexes contributed from TCNQ, but also high hydrophobicity *via* hydrophobic fluorine atom incorporation and metal cation elimination.[11] As an effective hydrophobic p-type dopant, F4-TCNQ has been recently introduced to replace conventional dopants (*e.g.*, LiTFSI and *t*BP) of spiro-OMeTAD[12] for the fabrication of MAPbI$_3$-based (MA = CH$_3$NH$_3$) PSCs. The use of F4-TCNQ indeed enabled a promising stabilization of the devices by effectively protecting the perovskite layer, owing to the intrinsic hydrophobic character of F4-TCNQ, as also observed for other types of PSCs using spiro-OMeTAD as the HTM.[13,14] Since then, F4-TCNQ has been investigated as a dopant for other HTMs,[15] *i.e.*, PTAA,[16] poly(3,4-ethylene dioxythiophene) polystyrene sulfonate (PEDOT : PSS),[17] and poly(3-hexylthiophene) (P3HT)[18] to enhance the stability and efficiency of both standard (n-i-p) and inverted (p-i-n) PSC structures. Surprisingly, there is still no application of F4-TCNQ in the currently most popular PSC architecture, *i.e.*, the n-i-p mesoporous structure based on triple cation and mixed halide (Cs$_{0.05}$FA$_{0.81}$MA$_{0.14}$PbI$_{2.55}$Br$_{0.45}$, CsFAMA) perovskite.[19] Furthermore, a clear elucidation of how F4-TCNQ influences the stability of unencapsulated devices by thoroughly correlating their photovoltaic parameters to charges in transfer dynamics, morphology, and charge conductivity is still missing in the literature.

In this work, to better understand the device degradation mechanisms, we select the hydrophobic F4-TCNQ as the sole dopant of spiro-OMeTAD HTM as a model system in contrast to the conventional hygroscopic dopants (*i.e.*, LiTFSI, *t*BP, and FK209) employed in the best-performing PSCs (see the chemical structures of the different dopants in Scheme 1). The corresponding n-i-p PSCs based on CsFAMA perovskite exhibit extremely high stability, retaining above 85% of their initial PCEs after nearly 10 months (monitoring period) of shelf-storage in air (darkness, RH $\sim$ 40%) with an estimated T_{80} lifetime of $\sim$380 days. On the contrary, the performance of the devices containing spiro-OMeTAD with conventional dopants drops to about 50% of its initial values during the same period. Importantly, the absolute PCE values (>11%) of F4-TCNQ-doped
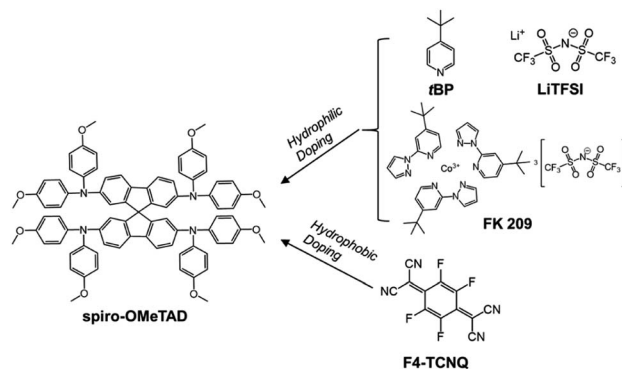
Scheme 1 Chemical structures of spiro-OMeTAD and the different dopants used in this work.

devices exceed those (<10%) of conventionally doped PSCs after 160 days of shelf storage, which suggests that F4-TCNQ is a more promising dopant for practical applications of PSCs. It was found that the stability of the devices is mainly related to changes in the fill factor over time. We relate these changes to the conductivity, morphology, and interface properties of the spiro-OMeTAD layer. We suggest that F4-TCNQ maintains a more uniform conductivity, whereas we see the indication of a detrimental doping profile using standard dopants. Time-resolved photoluminescence (TRPL) measurements indicate that F4-TCNQ doping of spiro-OMeTAD films effectively slows down the degradation of charge transfer kinetic characteristics over a monitored time of 7 weeks, while conductivity measurements and device simulations show that charge extraction remains good for F4-TCNQ doped devices over long-time scales. Our study suggests that the F4TCNQ p-dopant promotes the hydrophobicity-induced stability of the underlying perovskite layer (as discussed in earlier literature) and the stability of the spiro-OMeTAD layer itself and that of the perovskite/HTM interface.

Results and discussion

Influence of dopants on interfacial charge transfer dynamics

To evaluate the influence of HTM (spiro-OMeTAD) dopants on the charge transfer dynamics at the perovskite/spiro-OMeTAD interface, we prepared four kinds of samples with differently doped spiro-OMeTAD films: (i) glass/CsFAMA/undoped spiro-OMeTAD, (ii) glass/CsFAMA/*t*BP : LiTFSI doped spiro-OMeTAD, (iii) glass/CsFAMA/*t*BP : LiTFSI : FK209 doped spiro-OMeTAD (reference), (iv) glass/CsFAMA/F4-TCNQ (2%, mol%) doped spiro-OMeTAD. We chose the 2 mol% concentration of F4-TCNQ in spiro-OMeTAD, sample (iv) because this concentration yielded the best device performance, as demonstrated in Solar cell performance. Fig. S1 in the ESI† shows the absorption spectra of the different samples. The spectral shape with a shoulder around 740 nm is consistent with previous reports on CsFAMA perovskite.[3] No obvious spectral change is observed among these samples, suggesting that the perovskite layer's thickness (*ca.* 500 nm) is nearly identical with a negligible impact from the spiro-OMeTAD dopants.

11722 | *J. Mater. Chem. A*, 2022, **10**, 11721–11731

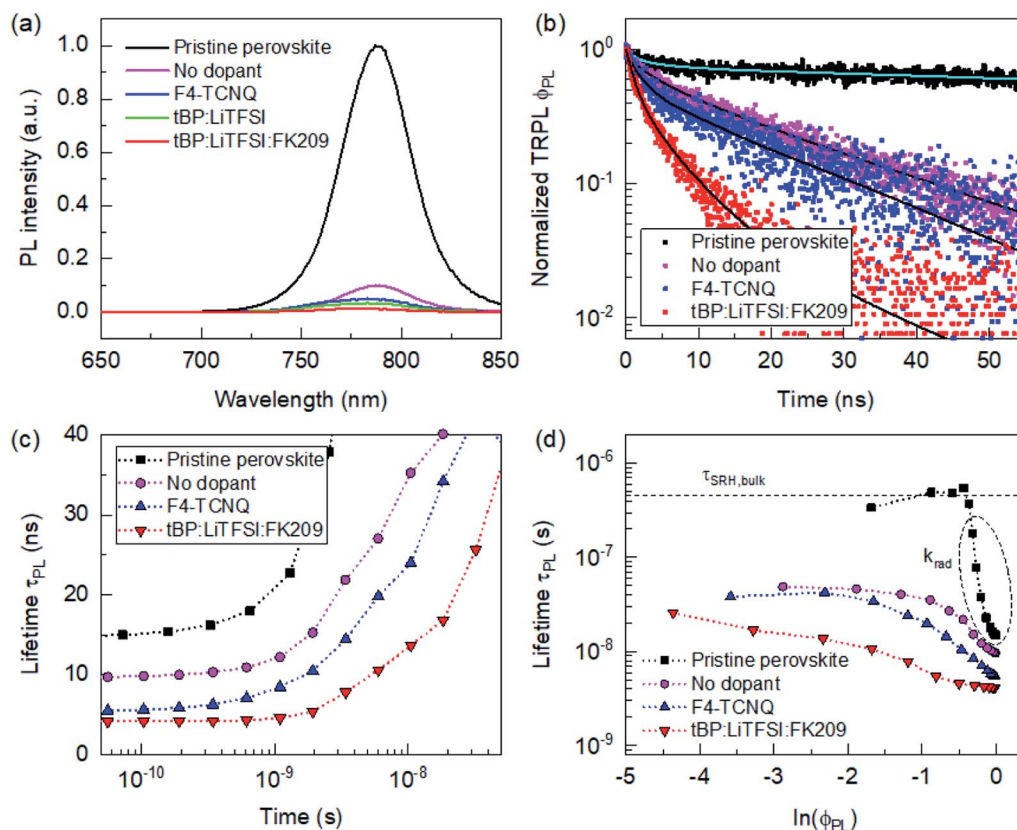This journal is © The Royal Society of Chemistry 2022

Fig. 1 Photoluminescence (PL) of pure perovskite films on glass and glass/perovskite/spiro-OMeTAD layer stacks. (a) Steady-state PL spectra. (b) Time-resolved PL (TRPL) for an excitation wavelength of 483 nm, monitored at 765 nm. Solid lines represent a rigorous smoothing of the raw data using a non-parametric spline fit in combination with moving average filtering. (c) Differential lifetime τ_{PL} calculated from the smoothed TRPL data according to eqn (1). (d) Differential lifetime as a function of the logarithm of the TRPL intensity, which serves as a relative measure of the quasi-Fermi level splitting, $\ln(\phi_{PL}) \propto \Delta E_F$. The plateau of τ_{PL} seen for the pristine perovskite sample was used to estimate the Shockley Read Hall (SRH) lifetime $\tau_{SRH,bulk}$ in the bulk.

Fig. 1a shows the photoluminescence (PL) spectra of the samples together with a reference, consisting of a pristine perovskite layer on glass (glass/CsFAMA) for comparison. A strong PL signal centered at around 765 nm is observed for the reference sample (glass/CsFAMA) because no expected charge transfer reaction occurs after exciting the perovskite at 483 nm in the excited state. All glass/CsFAMA/spiro-OMeTAD films exhibit an obvious quench of the perovskite PL with a variation among the differently doped spiro-OMeTAD films. It is known that the PL quenching capability of spiro-OMeTAD is enhanced upon more effective doping of spiro-OMeTAD. Dopants such as Co(III)-complex (FK209) have been reported to significantly deepen the highest occupied molecular orbital (HOMO) level of spiro-OMeTAD,[20] leading to a refined energy level alignment with the valence band of the perovskite layer and consequently to improved hole extraction at the perovskite/doped spiro-OMeTAD. By comparing the PL amplitude of the spiro-OMeTAD containing samples (glass/CsFAMA/spiro-OMeTAD) with the glass/CsFAMA reference, the hole injection yield is estimated for differently doped spiro-OMeTAD films and summarized in Table 1. The reference sample (spiro-OMeTAD doped with tBP : LiTFSI : FK209) shows the highest hole injection yield (98.8%) as expected, while the F4-TCNQ-doped

sample also has a reasonably high hole injection yield of 96.5%.[21]

To clarify the influence of the various spiro-OMeTAD dopants on the hole transfer dynamics, we monitored the TRPL decays for these as-deposited samples by conducting time-correlated single-photon counting (TCSPC) measurements (for experimental details, see ESI†). The comparison of the various PL decays is shown in Fig. 1b. We analyzed the TRPL decays in terms of the differential lifetime

$$\tau_{PL} = \left(-\frac{1}{m} \frac{d\ln(\phi_{PL})}{dt} \right)^{-1} \qquad (1)$$

Table 1 Hole injection yields estimated from the PL quenching and surface recombination velocities from the TRPL data for perovskite films with an HTM of spiro-OMeTAD with different dopants

Dopants in spiro-OMeTAD	Hole injection yield (%)	Surface recombination velocity (cm s^{-1})
No dopant	91.7	1800
F4-TCNQ	96.5	2400
tBP : LiTFSI	97.4	—
tBP : LiTFSI : FK209	98.8	3600

This journal is © The Royal Society of Chemistry 2022

J. Mater. Chem. A, 2022, **10**, 11721–11731 | **11723**

where $\phi_{PL}(t)$ is the TRPL intensity at a given time after the pulse excitation and the m a factor related to the injection level.[22–24] Here, we set $m = 2$ for high-level injection, assuming the perovskite layer to be intrinsic or sufficiently low doped.[24] As the calculation of τ_{PL} requires the derivative of a noisy signal, rigorous smoothing of the measured transients is required. For this purpose, we used a non-parametric spline fit in combination with moving average filtering (see lines in Fig. 1b). In Fig. 1c, the differential lifetime is plotted as a function of time. It can be clearly seen that τ_{PL} is not constant but rather varies strongly over the course of the TRPL decay. Hence, a simple exponential fit would not be suitable to capture all relevant features. From Fig. 1b and c it is readily seen that the TRPL decay is accelerated by the presence of an HTM, which indicates the occurrence of an interfacial hole transfer. The fastest decay is displayed by the sample with the spiro-OMeTAD doped with tBP : LiTFSI : FK209, followed by the spiro-OMeTAD doped with F4-TCNQ and the undoped spiro-OMeTAD.

For a deeper analysis of the TRPL decays and decouple effects in bulk and at the interface, we used an alternative representation of the data recently proposed by Krückemeier et $al.$[24] The authors have shown that it is advantageous to plot the lifetime as a function of the quasi-Fermi level splitting $\Delta E_F = k_B T \ln(\Delta n^2 / n_i^2)$, where $k_B T$ is the thermal energy, Δn the excess carrier density, and n_i the intrinsic carrier density. Because ΔE_F scales directly with Δn, this representation is better suited to analyze recombination and extraction processes that depend on carrier density but not necessarily on time. As the absolute values of Δn and n_i are not known from the given experiments, we use the fact that the PL intensity scales with ΔE_F according to

$$\phi_{PL} \propto \exp\left(\frac{\Delta E_F}{k_B T}\right) \qquad (2)$$

which implies that $\ln(\phi_{PL})$ can be used as a relative measure of the quasi-Fermi level splitting.[24,25] Fig. 1d shows this representation for the four samples under test. For the pure perovskite film, two regimes can be distinguished: a carrier density-dependent lifetime at high PL signals (short delay times) and a constant lifetime at low PL signals (long delay times). Such a shape is typical for lead-halide perovskite films and agrees with numerical simulations.[24] We assign the density-dependent part to direct radiative recombination, a second-order process that scales with $k_{rad}\Delta n^2$, where k_{rad} is the radiative recombination coefficient. The constant part is associated with the (slower) recombination via traps, which according to Shockley Read Hall (SRH) statistics resembles a pseudo-first-order process. The plateau corresponds to an effective SRH lifetime in the bulk of $\tau_{SRH,bulk} \approx 460$ ns, which is a reasonable value for this type of perovskite absorbers.[26]

For the samples with an HTM, the TRPL decay is sped up over the whole range of carrier densities/quasi-Fermi level splittings. The acceleration at high densities (short delay times) indicates that the holes transfer to the HTM, decreasing the excess carrier density in the perovskite (quenching). At longer times, the decay is faster than for the neat perovskite, indicating an additional recombination channel, which can be attributed to interfacial recombination.[22,24,27] The plateau on which τ_{PL}

saturates is in this case given by a complex interplay of the bulk SRH lifetime, the surface recombination velocity S, and the energy level offset at the interface. The given data do not allow to clearly attribute the differences between the HTMs to a variation of either S or the energy levels. Assuming that the different dopants have similar effect on HOMO level of spiro-OMeTAD, it would be possible to estimate the magnitude of S using an effective lifetime approach[24]

$$\tau_{SRH,eff} = \left(\frac{1}{\tau_{SRH,bulk}} + \frac{1}{\tau_{SRH,surf}}\right)^{-1} = \left(\frac{1}{\tau_{SRH,bulk}} + \frac{S}{2d}\right)^{-1} \qquad (3)$$

where $d \approx 500$ nm is the thickness of the perovskite layer. This would lead to $S \approx 1800$–3600 cm s^{-1} (see Table 1), suggesting that hole extraction is fastest for the spiro-OMeTAD doped with tBP : LiTFSI : FK209.

Solar cell performance

We employed F4-TCNQ as the sole dopant in spiro-OMeTAD in standard mesoporous n-i-p PSCs with CsFAMA perovskite. The complete PSC structure is FTO/c-TiO$_2$/m-TiO$_2$/CsFAMA/spiro-OMeTAD (with and without dopants)/Au (see the detailed fabrication procedure in the ESI†), as illustrated in Fig. 2a. The thicknesses of each layer of the devices, estimated from cross-sectional scanning electron microscopy (SEM) images (see Fig. 2b), are consistent with those reported in previous works.[19] No significant difference is observed among the differently doped devices, indicating that the perovskite thickness (~500 nm) is nearly identical in each sample, independent of the various dopants in the spiro-OMeTAD layer.

We first optimized the concentration of F4-TCNQ in the spiro-OMeTAD solution to aim at the best device performance. The performance of the champion PSCs, where spiro-OMeTAD is doped with F4-TCNQ at different concentrations (1–6 mol%), is summarized in Table S1 in the ESI.† The device doped with 2 mol% of F4-TCNQ in spiro-OMeTAD exhibits the highest PCE of 14.6% with an average PCE of 13.3 ± 1.0%, mainly due to the superior V_{oc} (1.09 V) and FF (64.8%) compared to the other devices (with different mol% of F4-TCNQ). This suggests that the variable doping level of F4-TCNQ significantly influences the conductivity in the spiro-OMeTAD layer, as similarly observed in previous studies.[12] Additionally, PSCs with spiro-OMeTAD doped with tBP : LiTFSI, tBP : LiTFSI : FK209 (reference), and with undoped spiro-OMeTAD were fabricated for comparison using an identical procedure. Fig. 3 shows the comparison of current density (J)–voltage (V) curves of the champion devices based on the differently doped spiro-OMeTAD films, recorded under 1 sun illumination (AM 1.5 G, 100 mW cm^{-2}), both under forward and reverse bias scans. The average device performance (24 devices each), together with the standard deviation, and the photovoltaic parameters of the champion cells, are summarized in Table 2. Although the performance of F4-TCNQ-doped devices (average PCE: 13.44%) is lower than that of the reference cells (average PCE: 18.70%), where spiro-OMeTAD is conventionally doped with tBP : LiTFSI : FK209 as predicted, the PCE of the champion cell (14.57%) is still one of the highest values reported for standard n-i-p
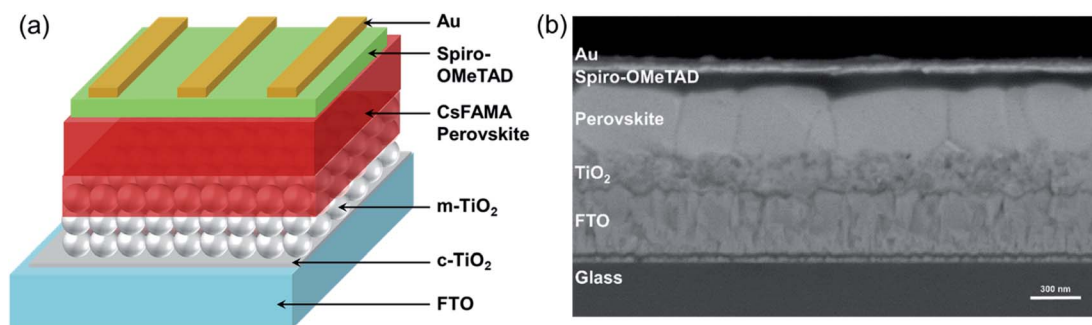
Fig. 2 (a) Schematic of mesoporous n-i-p CsFAMA perovskite solar cells as used in this work. (b) Cross-sectional SEM image for a typical solar cell fabricated in this work.
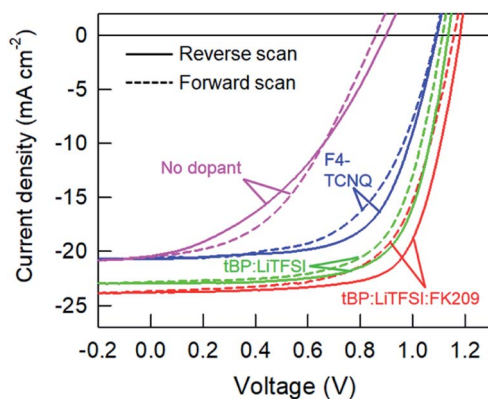

Fig. 3 J–V curves of the best devices with differently doped spiro-OMeTAD HTM under forward and reverse scans. The scan rate is 20 mV s^{-1}.

devices, where F4-TCNQ is employed as the sole dopant in spiro-OMeTAD.[28] The relatively low conductivity of F4-TCNQ-doped spiro-OMeTAD results in lower FF than that of reference devices, which will be experimentally determined in the following section. As a result, the PCE of F4-TCNQ-based devices is also lower than that of reference devices. However, a reduction of the hysteresis in the J–V curves of the F4-TCNQ-doped cell (Fig. 3) is observed compared to the case of conventionally doped cells (either tBP : LiTFSI : FK209 or tBP : LiTFSI), as quantitively evaluated by the decrease in the hysteresis index (H-index) in Table 2. In addition, we have extracted the series (R_S) and shunt (R_{SH}) resistances of the

devices from the dark J–V curves using the common 1-diode model,[29] as summarized in Table 2. It is known that the FF is influenced by both R_S and R_{SH}, with lower R_S and higher R_{SH} being required for improving the FF.[30] The F4-TCNQ-doped devices show higher R_S and lower R_{SH} compared to the reference devices, corresponding to an overall lower FF.

Stability study

Device stability. We then studied the stability of unencapsulated PSCs with differently doped spiro-OMeTAD by analyzing the variation of the photovoltaic parameters for the champion devices in shelf-storage conditions (darkness, RH ∼ 40%) as a function of storage time (Fig. 4). The cells doped with F4-TCNQ exhibit very high stability, retaining more than 85% of the initial PCE after nearly 300 d of storage (see Fig. 4a) with an estimated T_{80} of ∼380 d based on a linear projection of the stability trend from the peak PCE point (see the inset in Fig. 4a), which is one of the longest monitoring periods based on reported stability studies for PSCs.[31,32] In contrast, the traditionally doped devices (spiro-OMeTAD doped with tBP : LiTFSI : FK209 or with tBP : LiTFSI) degrade much more severely, retaining only 51% and 62% of their peak PCEs under identical storage conditions, respectively. Initial growth of the PCE achieving the maximum point within one week is observed for both cases of conventional dopants (tBP : LiTFSI : FK209 and tBP : LiTFSI), owing to a slow increase of V_{oc} (see Fig. 4b) at the initial stage of storage. The PCE trend of F4-TCNQ-based devices is most strongly affected by the changing FF while J_{sc} and V_{oc} remain fairly constant, apart from the initial V_{oc} increase, as evident in Fig. 4c. The FF gradually increases at

Table 2 Performance of perovskite solar cells with differently doped spiro-OMeTAD HTMs. All data are obtained from the reverse scan

Dopants in spiro-OMeTAD	PCE (%)	J_{sc} (mA cm^{-2})	V_{oc} (V)	FF (%)	H-index[a]	R_S (Ω cm^2)	R_{SH} (kΩ cm^2)
tBP : LiTFSI : FK209	18.3 ± 1.1 (19.9)[b]	22.3 ± 0.7 (23.6)	1.14 ± 0.02 (1.18)	70.5 ± 0.7 (71.8)	1.19 ± 0.03 (1.12)	5.9 ± 0.5 (5.0)	6.1 ± 0.5 (7.1)
tBP : LiTFSI	16.5 ± 0.9 (18.0)	21.9 ± 0.6 (22.9)	1.09 ± 0.01 (1.13)	68.1 ± 0.9 (69.5)	1.15 ± 0.03 (1.10)	6.4 ± 0.4 (5.7)	5.9 ± 0.5 (6.7)
F4-TCNQ	13.3 ± 1.0 (14.6)	19.5 ± 0.6 (20.7)	1.05 ± 0.02 (1.09)	63.4 ± 1.0 (64.8)	1.09 ± 0.01 (1.05)	7.0 ± 0.4 (6.3)	5.5 ± 0.6 (6.6)
Dopant-free	6.2 ± 1.2 (7.9)	18.9 ± 1.1 (20.5)	0.79 ± 0.02 (0.85)	43.4 ± 1.3 (45.3)	1.10 ± 0.02 (1.06)	31.1 ± 0.9 (29.6)	0.6 ± 0.4 (1.2)

[a] H-index is calculated as PCE$_{rev}$/PCE$_{for}$, where PCE$_{rev}$ and PCE$_{for}$ present PCEs measured under reverse and forward scans, respectively. [b] The values in brackets represent the parameters of the champion device.
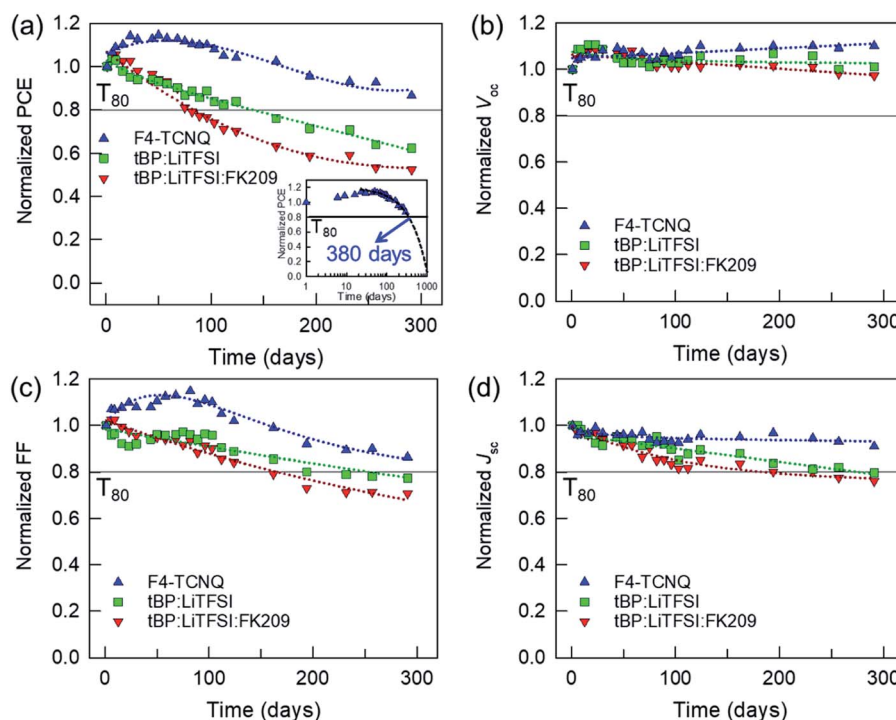
This journal is © The Royal Society of Chemistry 2022

J. Mater. Chem. A, 2022, **10**, 11721–11731 | **11725**

Fig. 4 Normalized photovoltaic parameters, (a) PCE, (b) V_{oc}, (c) FF, (d) J_{sc}, of the champion devices with differently doped spiro-OMeTAD *vs.* storage time, stored in air (darkness, RH ~ 40%). T_{80} represents the time when one photovoltaic parameter value decreases to 80% of its initial one. Inset in (a) represents the linear projection of the stability trend to extract the T_{80} shelf-lifetime (~380 days) of F4-TCNQ doped devices.

first, reaching a maximum value at about 20 d after the device fabrication. This FF-dominated PCE evolution is also observed for the device with undoped spiro-OMeTAD (see Fig. S2 in the ESI†).

Along with the gradual increase of FF, the PCE dramatically increases to a maximum of ~12.01% (initial PCE: 3.64%) after about 80 d storage in air, in good agreement with the previously observed long self-doping process required for the PCE growth of PSCs with undoped HTMs.[33] The J_{sc} of the F4-TCNQ-based cells retains above 95% of the initial value after nearly 10 months while those of the other two cases (reference and *t*BP : LiTFSI dopants) decrease to below 80% of their initial values (Fig. 4d). It is noteworthy that the hysteresis of both reference and F4-TCNQ doped devices reduces with H-indexes decreasing towards 1.0 after 50 days storage in air (data are not shown here), indicating that the hysteresis is not the main factor that influences device stability in this work. We have also assessed the long-term unencapsulated device stability under continuous white LED illumination (without UV light filter) in air by conducting maximum power point tracking (MPPT) measurements with three types of doped spiro-OMeTAD layers, *i.e.* dopant-free devices, reference devices (doped with *t*BP : LiTFSI : FK209), and F4-TCNQ-doped devices (6 cells for each case, see the MPPT measurement details in the ESI†). An initial increase in FF is observed under the illumination up to about 40 h for the F4-TCNQ-doped cells, which consistently show the highest FF (see Fig. S3 in the ESI†), compared to the other two cases (reference and dopant-free cells). This is in good

agreement with the observed FF-dominated shelf-stability for reference and F4-TCNQ doped devices.

More importantly, we found that the absolute PCE of the champion cell with F4-TCNQ-doped spiro-OMeTAD has surpassed those of the devices with conventionally doped spiro-OMeTAD after about 160 d of storage in the air. Fig. 5a–c shows the comparison between the *J–V* curves of fresh and aged devices after 295 d of storage for each dopant case. The PCE (11.78%) of the aged champion cell doped with F4-TCNQ constitutes a 26% and 11% performance enhancement compared to those of the aged reference cell (9.35%) and *t*BP : LiTFSI doped cell (10.66%), respectively. This suggests that F4-TCNQ is a more suitable option than the well-known spiro-OMeTAD additives when considering practical applications requiring good long-term stability. To confirm the surface property of the HTM film coated on perovskite, we measured water contact angles (CAs) for glass/CsFAMA/differently doped spiro-OMeTAD samples (Fig. 5d–f) and the obtained CA values are summarized in Table S2 in the ESI.† The mean CA (86.5°) of the F4-TCNQ doped spiro-OMeTAD film is higher than those of reference doped (65.8°) and *t*BP : LiTFSI doped (77.0°) HTM films, emphasizing the hydrophobicity of F4-TCNQ dopant that can effectively prevent the degradation of the perovskite layer from moisture penetration.

To assess the thermal stability of the devices doped with F4-TCNQ *vs.* the conventionally doped counterparts, we evaluated the PCEs before and after heating the PSCs at 65 °C for 12 h in nitrogen atmosphere[19,34] (Fig. S5†). The F4-TCNQ doped device retains 96% of its initial PCE upon heating, while the
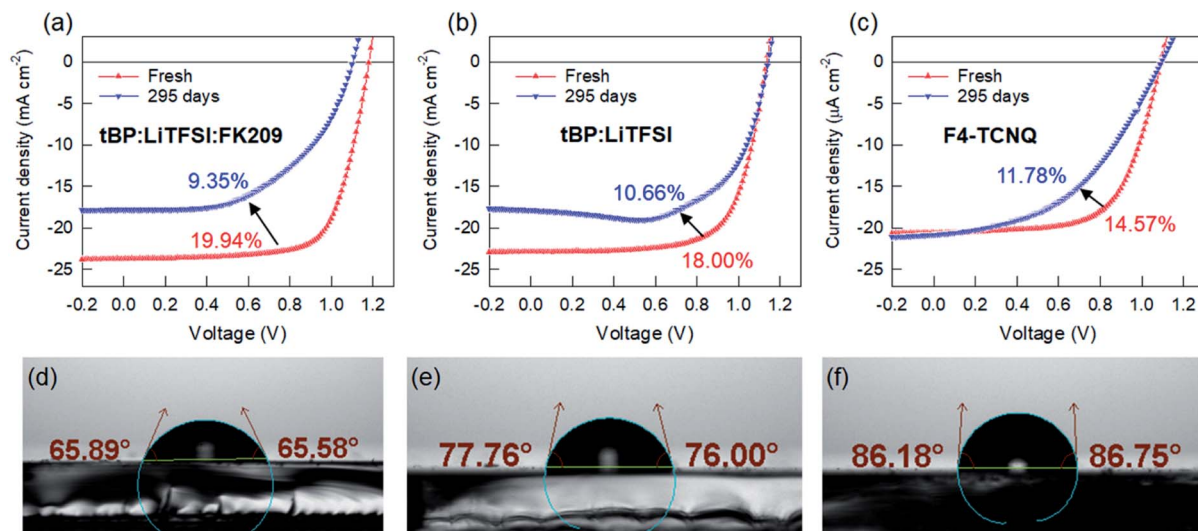
11726 | *J. Mater. Chem. A*, 2022, **10**, 11721–11731

This journal is © The Royal Society of Chemistry 2022

Fig. 5 (a–c) Comparison of $J-V$ curves of fresh and aged devices with differently doped spiro-OMeTAD layers. The scan rate is 20 mV s^{-1}. Water contact angles (CAs) for differently doped spiro-OMeTAD layers on perovskite films: (d) tBP : LiTFSI : FK209, (e) tBP : LiTFSI, (f) F4-TCNQ.

performance of the reference device with conventional dopants (tBP : LiTFSI : FK209) decreases to ~90% of its initial value. This suggests that the F4-TCNQ dopant also possesses higher thermal tolerance than the reference dopants.

Storage-time dependent TRPL. To further explore the degradation mechanism and correlate it to the interfacial charge transfer dynamics, we measured storage-time dependent TRPL decays for glass/CsFAMA/spiro-OMeTAD samples with different doping in the HTM and compared with a pristine CsFAMA film on glass as the control sample. Fig. S6 in ESI† shows the raw TRPL data. For the pure perovskite film, the TRPL decay remains relatively unchanged over the first 7 weeks of storage but is strongly accelerated after 9 weeks. This indicates that a degradation process starts in the perovskite film after this time, and we decided to limit our analysis to 7 weeks of shelf storage. Fig. 6 shows the variation of the differential lifetime τ_{PL} over storage time for the different samples. As can be seen from the pristine perovskite (Fig. 6a), the SRH lifetime in the bulk ($\tau_{SRH,bulk}$) remains approximately constant, and only minor fluctuations occur in the direct radiative recombination (k_{rad}). We, therefore, assume that the clear trends with storage time seen in the samples with spiro-OMeTAD are related to the dynamics at the interface and not in the bulk of the perovskite film. For the sample with the tBP : LiTFSI : FK209-doped spiro-OMeTAD (Fig. 6b), the lifetime is gradually reduced after 1 week storage. Given that τ_{PL} still reflects the charge transfer over the perovskite/HTM interface; this indicates a general slow-down of charge extraction and subsequent interfacial recombination with storage time. The behavior with storage time is notably different for the spiro-OMeTAD doped with F4-TCNQ (Fig. 6c) and the undoped spiro-OMeTAD (Fig. 6d). For these samples, the charge transfer is first accelerated after 1 week of storage and then slows down again; only after 5 weeks are the determined lifetimes longer than for the fresh samples. The variation of the TRPL decay is in good agreement with the evolution of the FF for the F4-TCNQ-doped device, which achieves the highest

value after about 20 days of storage (Fig. 4c). This further confirms that the self-doping (dopant-free) or slow doping process (F4-TCNQ) in ambient conditions in spiro-OMeTAD film influences both interfacial hole injection kinetics and hole transport within the HTM, in relation to the stability decay rate of their corresponding devices.

Conductivity. Four-point probe conductivity measurements were performed on thin films of spiro-OMeTAD doped with either tBP : LiTFSI : FK209 or 2 mol% F4-TCNQ to clarify how the degradation of the bulk conductivity in the HTM with time influences the solar cell device performance. Sections 1.2 and 1.4 in the ESI† give details about device fabrication for the conductivity measurements, the experimental setup and the measurements. The doped spiro-OMeTAD films were stored either in a nitrogen-filled glovebox, dry air or in ambient conditions for eight months. During this time, conductivity measurements were carried out by transferring samples into a nitrogen-filled glovebox for the duration of the measurements, regardless of the storage conditions. The change in conductivity as a function of storage time is shown in Fig. 7. The conductivity of fresh tBP : LiTFSI : FK209-doped films is almost an order of magnitude higher than that of fresh F4-TCNQ-doped films. Films stored in nitrogen and dry air show a similar slow degradation of the conductivity with storage time for both doping protocols. Films stored in ambient conditions act quite differently depending on the dopant used. The tBP : LiTFSI : FK209-doped film shows an initial increase in conductivity with almost a factor of four after ten days in ambient conditions. On the other hand, the conductivity of the F4-TCNQ-doped film decreases steadily with time during the first two months, reaching a rather constant value from two months onwards. The initial increase in conductivity for the tBP : LiTFSI : FK209-doped film can be attributed to the presence of moisture in the air, which has been shown to give rise to a redistribution of LiTFSI in the layer and a concomitant increase in conductivity.[35] Except for the tBP : LiTFSI : FK209-
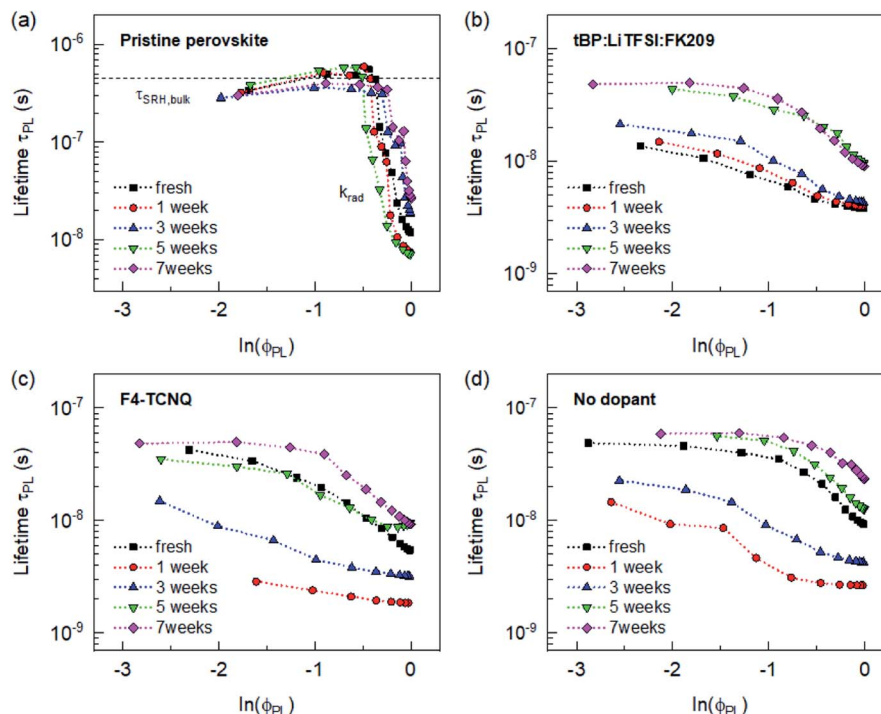
Fig. 6 Differential lifetimes τ_{PL} derived from TRPL decays measured after different shelf-storage times for (a) a pure perovskite film on glass and (b–d) glass/perovskite/spiro-OMeTAD layer stacks with different dopant combinations, excited at 483 nm, and monitored at 765 nm. All films were stored in air (darkness, RH ∼ 40%).
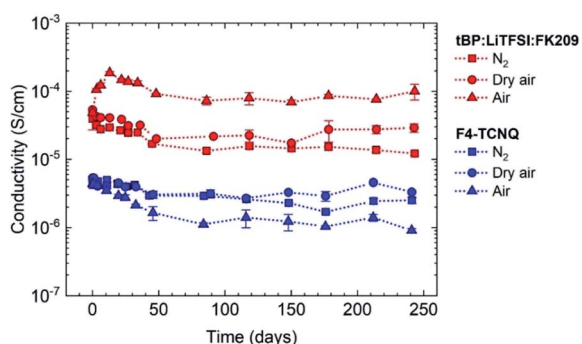

Fig. 7 Storage time-dependent conductivity of spiro-OMeTAD films doped with either tBP : LiTFSI : FK209 or F4-TCNQ. Films were stored in a nitrogen-filled glovebox (N_2), dry air, or ambient air.

μm^2. After being aged at ambient conditions (RH ∼ 40%) for three months, the film remained uniform and flat with almost unchanged surface morphology (RMS of 0.4 nm). The unchanged morphology reveals that the spiro-OMeTAD film was not disrupted by being exposed to air when F4-TCNQ was used as the dopant, which indicates a good resilience to moisture and oxygen.

In contrast, a clear change in morphology after air exposure appeared for the spiro-OMeTAD doped with tBP : LiTF-SI : FK209. Round aggregates were found to cover the whole surface of the layer, leading to an increase in the RMS roughness of the film from 0.4 nm to 1.6 nm. The formation of the
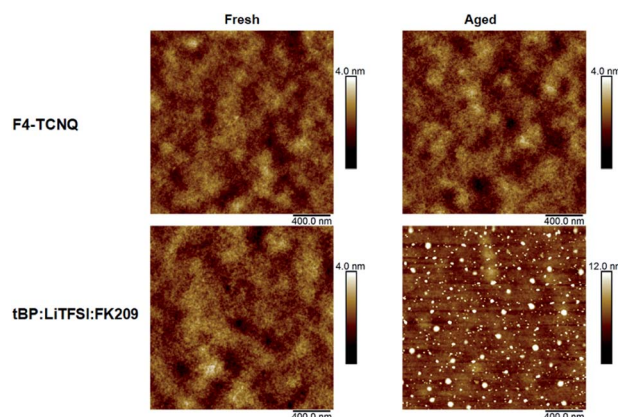
doped sample stored in air, all samples show a slightly faster decrease in conductivity during the first two months followed by a slower almost constant conductivity value for the rest of the storage time.

Morphological stability. To investigate the role of dopants in changing the morphology of the hole transport layer, we performed atomic force microscopy (AFM) imaging on spiro-OMeTAD films doped with F4-TCNQ compared to the reference sample with conventional dopants. Fig. 8 shows the AFM topography images of as-prepared and aged spiro-OMeTAD samples. The fresh spiro-OMeTAD sample with F4CNQ showed a very smooth surface at the nanoscale with a root-mean-square (RMS) value of 0.356 nm for an area of 2 × 2

Fig. 8 AFM images of the fresh and aged spiro-OMeTAD films with F4-TCNQ dopant and conventional dopants (tBP : LiTFSI : FK209).

segregations in the spiro-OMeTAD film by aging at ambient conditions is generally attributed to the agglomeration and hydrolysis of the conventional additive, LiTFSI.[36] The hygroscopic LiTFSI easily adsorbs water and oxygen, leading to aggregates of lithium salt and the degradation of the spiro-OMeTAD layer. Nevertheless, the hydrophobic F4-TCNQ dopant can effectively resist the adsorption of atmospheric moisture by avoiding the formation of aggregates within the spiro-OMeTAD layer. Although tBP is utilized in the spiro-OMeTAD layer as an additive to hinder the phase segregation of LiTFSI and provide a homogenous hole transport layer,[37,38] the evaporation of tBP will eventually cause the aggregation of the LiTFSI molecules. On the other hand, we speculate that the aggregation of the standard dopants towards the spiro-OMeTAD/anode (Au) interface is partially attributed to the diffusion of those light dopants within the spiro-OMeTAD away from the perovskite/HTM interface. This is in contrast to the observations on the films with spiro-OMeTAD doped with the bulkier F4-TCNQ. The change in morphology related to the inhomogeneous doping of spiro-OMeTAD is assumed to be detrimental to the performance and stability of the devices as it affects the quality of the HTM/perovskite interface and the charge extraction process.

Drift-diffusion simulations. To determine which degradation mechanisms could explain the measured time-evolution of the photovoltaic parameters for the F4-TCNQ- and tBP : LiTF-SI : FK209-doped devices, we performed extensive drift-diffusion simulations. We used a one-dimensional model including the spiro-OMeTAD, perovskite, and TiO$_2$ layers, utilizing a previously published drift-diffusion solver.[39] The simulation parameters used are shown in Table S3 in the ESI.†

The most significant change we observed during degradation is that of the FF and, to a lesser extent, the V_{oc}, and so we chose to focus on them in the simulations. Fig. 9a shows simulated J–V curves for different conductivities in the spiro-

OMeTAD layer, achieved by changing the doping concentration in the HTM. A large increase in FF can be seen for enhancing the conductivity from 8×10^{-7} S cm^{-1} to 8×10^{-6} S cm^{-1}, while the FF remains constant for conductivities larger than 8×10^{-6} S cm^{-1}. Increasing the doping concentration (and thus the conductivity) also increases V_{oc} due to the corresponding increase of the built-in potential. The measured conductivity for F4-TCNQ-doped samples was highest in fresh devices, at about 5×10^{-6} S cm^{-1}, and decreased to 9×10^{-7} S cm^{-1} after 250 days storage in air (Fig. 7). Based on the simulations, there should be a steady decrease in FF for this range of conductivities, which we indeed observed in the measured J–V data, see Fig. 4c. Therefore, we conclude that the loss in FF observed in F4-TCNQ-doped devices is a result of the degrading conductivity of the spiro-OMeTAD layer.

For the tBP : LiTFSI : FK209-doped films, the measurements yielded an initial conductivity of 5×10^{-5} S cm^{-1}, which further increased to 2×10^{-4} S cm^{-1} during the first ~20 days of storage. Based on the simulation data in Fig. 9a, there should be no change in FF for this variation in conductivity. Also, theoretical studies show that those conductivities are large enough to ensure charge extraction without any transport losses.[39,40] Thus, the degrading device performance of tBP : LiTF-SI : FK209-doped devices cannot be understood based on the measured change in conductivity. Instead, we looked at several other possible sources for the observed decrease in FF in the tBP : LiTFSI : FK209-doped devices. As shown in Fig. S7 in the ESI,† no significant decrease in FF was found when changing the energy offset between the perovskite and the spiro-OMeTAD layer, the radiative recombination coefficient, or the transfer velocity across the interface. A change in interface recombination lifetime by several orders of magnitude was found to decrease FF, but this is unlikely to be the cause given the relatively small changes observed in the TRPL lifetime (Fig. 6). However, we found that the measured changes in the interface
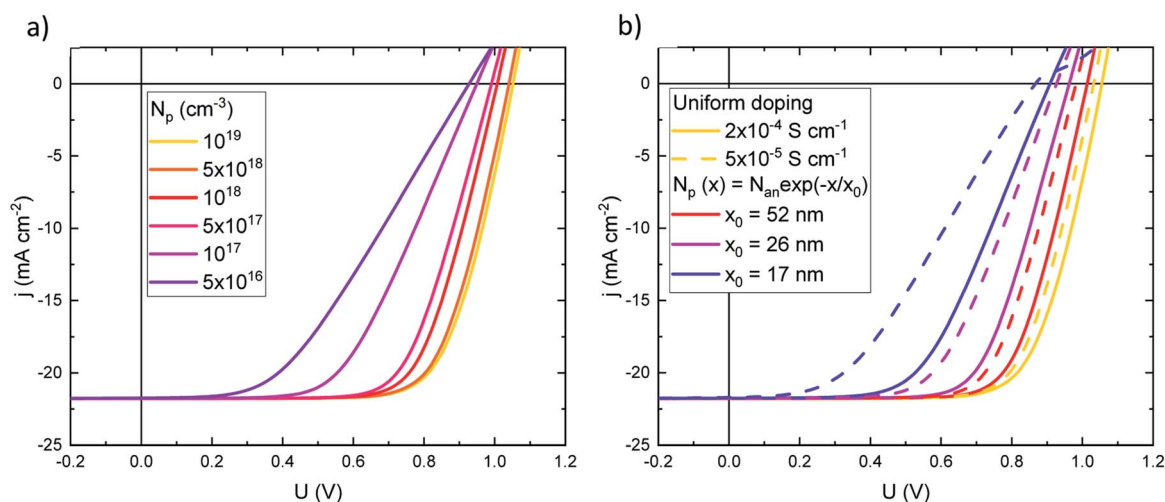

Fig. 9 Simulation data with varying (a) doping concentrations N_p in the spiro-OMeTAD layer and (b) exponential doping profiles $N_p(x) = N_{an}\exp(-x/x_0)$, and uniform doping for comparison. In (b), the full lines have $N_{an} = 1.25 \times 10^{19}$ cm^{-3} and the dashed lines $N_{an} = 3.12 \times 10^{18}$ cm^{-3}, corresponding to the highest and lowest measured conductivities measured for tBP : LiTFSI : FK209-doped films, 2×10^{-4} S cm^{-1} and 5×10^{-5} S cm^{-1}.

This journal is © The Royal Society of Chemistry 2022

J. Mater. Chem. A, 2022, **10**, 11721–11731 | **11729**

recombination lifetime within one order of magnitude could change V_{oc} by up to 40 mV (Fig. S7a†). Hence, from the TRPL data we can at least partially explain the trends in V_{oc} we observed in the stability measurements.

Because simple homogeneous material and interface properties cannot explain the observed trends in FF, we next investigated the effects of a non-uniform dopant distribution. The assumption of non-uniform doping was motivated by the migration and aggregation of dopants observed in the AFM measurements described above. Also, the increase in horizontally measured conductivity observed for tBP : LiTFSI : FK209-doped spiro-OMeTAD films stored in air supports a possible migration of dopants vertically inside the layer. To keep the number of unknown parameters at a minimum, we chose to use an exponential doping profile with the highest concentration at the anode N_{an} and decreasing as $N_p(x) = N_{an}\exp(-x/x_0)$, where x is the distance from the anode and x_0 determines how steep the profile is. Specifically, we looked at two different doping concentrations at the anode, corresponding to the highest and lowest measured conductivity for the tBP : LiTFSI : FK209-doped spiro-OMeTAD of 2×10^{-4} S cm^{-1} and 5×10^{-5} S cm^{-1}, respectively. Fig. 9b shows the results for different exponential profiles and compares it with the uniform case. As can be seen, the main impact of an increasingly non-uniform doping profile is on the FF with a small change in V_{oc}, which matches well the change in the J–V characteristics we observed for tBP : LiTFSI : FK209-doped devices. Therefore, we attribute these devices' degrading FF and V_{oc} mainly to migration of dopants towards the anode and/or aggregation of dopants with a concomitant decrease in doping efficiency adjacent to the perovskite.[41,42] The fact that this dopant migration does not happen with the hydrophobic F4-TCNQ dopant, as evident from the AFM images in Fig. 8, provides a reasonable explanation for the much better long-term stability of the solar cells with F4-TCNQ-doped spiro-OMeTAD as HTM. However, the underlying reason for the suppressed migration in the F4-TCNQ-case is not entirely clear. One possibility is that a hygroscopic dopant combined with moisture from the ambient migrates more easily than a hydrophobic one. This is supported by the reference device with standard dopants exhibiting a comparable moderate PCE drop ($\sim$11% of its initial value) compared to that ($\sim$6% of the initial PCE) of the F4-TCNQ doped device after nearly 11 months of storage in a dry cabinet (RH<10%), see Fig. S8 in the ESI.† An additional factor is that the F4-TCNQ might be less prone to migrate simply due to its larger and bulkier size.

Conclusions

In summary, we investigated the role of hydrophobic F4-TCNQ p-type doping of spiro-OMeTAD in the degradation of mesoporous triple-cation n-i-p PSCs by employing two different doping strategies, $i.e.$, conventional (tBP, LiTFSI, and FK209) $vs.$ F4-TCNQ. A comprehensive set of experimental and theoretical measures explored the underlying mechanisms of the high stability observed for F4-TCNQ doped devices, including TRPL analysis, conductivity measurements, morphological analysis,

and drift-diffusion simulations. When compared to conventionally doped ($e.g.$, tBP, LiTFSI, and FK209) devices, the F4-TCNQ doped PSCs exhibited remarkably high shelf-stability (stored in air, RH $\sim$ 40%), retaining more than 85% of the initial PCE after 300 days storage with an estimated T_{80} lifetime of about 380 days, which is to the best of our knowledge one of the longest shelf-lifetimes among all the reported types of PSCs. We found that the degradation is due mainly to the deterioration of the FF, and the F4-TCNQ doping even promotes the FF up to about 50 days of storage. In contrast, the FF of the reference devices gradually decreases from the very beginning of storage. More importantly, our results suggest that the long-term uniform doping of F4-TCNQ in the spiro-OMeTAD layer plays a central role in maintaining the high FF, by impeding dopant migration towards the anode, which easily occurs in devices employing conventional hygroscopic dopants. Our work not only provides a deep understanding of the degradation mechanism of standard mesoporous PSCs, but also paves the way for further development of highly stable devices through an effective doping engineering strategy for the HTM layer.

Author contributions

M. Liu: data curation, formal analysis, investigation, methodology, writing-original draft. S. Dahlström: conceptualization, data curation, formal analysis, methodology, writing-review & editing. C. Ahläng: data curation, formal analysis, investigation, software, writing-review & editing. S. Wilken: formal analysis, investigation, validation, writing-review & editing. A. Degterev: data curation, writing-review & editing. A. Matuhina: data curation, writing-review & editing. M. Hadadian: data curation, formal analysis, investigation, writing-review & editing. M. Markkanen: data curation, formal analysis. K. Aitola: data curation, formal analysis, investigation, writing-review & editing. A. Kamppinen: data curation, formal analysis. J. Deska: data curation, formal analysis. O. Mangs: data curation, formal analysis. M. Nyman: formal analysis, investigation, validation, writing-review & editing. P. D. Lund: funding acquisition, resources, supervision, writing-review & editing. J.-H. Smått: formal analysis, funding acquisition, resources, supervision, writing-review & editing. R. Österbacka: conceptualization, formal analysis, funding acquisition, project administration, resources, supervision, validation, writing-review & editing. P. Vivo: formal analysis, funding acquisition, investigation, project administration, resources, supervision, validation, visualization, writing-review & editing.

Conflicts of interest

There are no conflicts of interest to declare.

Acknowledgements

11730 | $J. Mater. Chem. A$, 2022, 10, 11721–11731

This journal is © The Royal Society of Chemistry 2022

References

1 J. Jeong, M. Kim, J. Seo, H. Lu, P. Ahlawat, A. Mishra, Y. Yang, M. A. Hope, F. T. Eickemeyer, M. Kim, Y. J. Yoon, I. W. Choi, B. P. Darwich, S. J. Choi, Y. Jo, J. H. Lee, B. Walker, S. M. Zakeeruddin, L. Emsley, U. Rothlisberger, A. Hagfeldt, D. S. Kim, M. Grätzel and J. Y. Kim, *Nature*, 2021, **592**, 381–385.

2 Z. Hawash, L. K. Ono and Y. Qi, *Adv. Mater. Interfaces*, 2018, **5**, 1700623.

3 M. Saliba, J.-P. Correa-Baena, C. M. Wolff, M. Stolterfoht, N. Phung, S. Albrecht, D. Neher and A. Abate, *Chem. Mater.*, 2018, **30**, 4193–4201.

4 Y. Cai, J. Cui, M. Chen, M. Zhang, Y. Han, F. Qian, H. Zhao, S. Yang, Z. Yang, H. Bian, T. Wang, K. Guo, M. Cai, S. Dai, Z. Liu and S. Liu, *Adv. Funct. Mater.*, 2021, **31**, 2005776.

5 K. Rakstys, C. Igci and M. K. Nazeeruddin, *Chem. Sci.*, 2019, **10**, 6748–6769.

6 T. Miyasaka, A. Kulkarni, G. M. Kim, S. Öz and A. K. Jena, *Adv. Energy Mater.*, 2020, **10**, 1902500.

7 S. Wang, Z. Huang, X. Wang, Y. Li, M. Günther, S. Valenzuela, P. Parikh, A. Cabreros, W. Xiong and Y. S. Meng, *J. Am. Chem. Soc.*, 2018, **140**, 16720–16730.

8 W. Li, H. Dong, L. Wang, N. Li, X. Guo, J. Li and Y. Qiu, *J. Mater. Chem. A*, 2014, **2**, 13587–13592.

9 B. Xu, J. Huang, H. Ågren, L. Kloo, A. Hagfeldt and L. Sun, *ChemSusChem*, 2014, **7**, 3252–3256.

10 Q. Wang, *Phys. Chem. Chem. Phys.*, 2018, **20**, 10114–10120.

11 T. H. Schloemer, J. A. Christians, J. M. Luther and A. Sellinger, *Chem. Sci.*, 2019, **10**, 1904–1935.

12 J. Luo, C. Jia, Z. Wan, F. Han, B. Zhao and R. Wang, *J. Power Sources*, 2017, **342**, 886–895.

13 L. Huang, Z. Hu, J. Xu, K. Zhang, J. Zhang, J. Zhang and Y. Zhu, *Electrochim. Acta*, 2016, **196**, 328–336.

14 M. A. Mahmud, N. K. Elumalai, M. B. Upama, D. Wang, V. R. Gonçales, M. Wright, C. Xu, F. Haque and A. Uddin, *Phys. Chem. Chem. Phys.*, 2017, **19**, 21033–21045.

15 S. Yang, H. Zhao, M. Wu, S. Yuan, Y. Han, Z. Liu, K. Guo, S. Liu, S. Yang, H. Zhao, S. Yuan, Y. Han, Z. Liu, S. Liu, M. Wu and K. Guo, *Sol. Energy Mater. Sol. Cells*, 2019, **201**, 110052.

16 F. Zhang, J. Song, R. Hu, Y. Xiang, J. He, Y. Hao, J. Lian, B. Zhang, P. Zeng and J. Qu, *Small*, 2018, **14**, 1704007.

17 D. Liu, Y. Li, J. Yuan, Q. Hong, G. Shi, D. Yuan, J. Wei, C. Huang, J. Tang and M. K. Fung, *J. Mater. Chem. A*, 2017, **5**, 5701–5708.

18 H. C. V. Tran, W. Jiang, M. Lyu and H. Chae, *J. Phys. Chem. C*, 2020, **124**, 14099–14104.

19 H. Zhang, M. Liu, W. Yang, L. Judin, T. I. Hukka, A. Priimagi, Z. Deng and P. Vivo, *Adv. Mater. Interfaces*, 2019, **18**, 1901036.

20 H. Nishimura, N. Ishida, A. Shimazaki, A. Wakamiya, A. Saeki, L. T. Scott and Y. Murata, *J. Am. Chem. Soc.*, 2015, **137**, 15656–15659.

21 S. Makuta, M. Liu, M. Endo, H. Nishimura, A. Wakamiya and Y. Tachibana, *Chem. Commun.*, 2016, **52**, 673–676.

22 B. Krogmeier, F. Staub, D. Grabowski, U. Rau and T. Kirchartz, *Sustainable Energy Fuels*, 2018, **2**, 1027–1034.

23 T. Kirchartz, J. A. Márquez, M. Stolterfoht and T. Unold, *Adv. Energy Mater.*, 2020, **10**, 1904134.

24 L. Krückemeier, B. Krogmeier, Z. Liu, U. Rau and T. Kirchartz, *Adv. Energy Mater.*, 2021, **11**, 2003489.

25 P. Würfel, *Physics of Solar Cells: from Principles to New Concepts*, John Wiley and Sons, 2007.

26 M. Liu, M. Endo, A. Shimazaki, A. Wakamiya and Y. Tachibana, *ACS Appl. Energy Mater.*, 2018, **1**, 3722–3732.

27 M. Stolterfoht, C. M. Wolff, J. A. Márquez, S. Zhang, C. J. Hages, D. Rothhardt, S. Albrecht, P. L. Burn, P. Meredith, T. Unold and D. Neher, *Nat. Energy*, 2018, **3**, 847–854.

28 S. Li, Y. L. Cao, W. H. Li and Z. S. Bo, *Rare Met.*, 2021, **40**, 2712–2729.

29 S. Yoo, B. Domercq and B. Kippelen, *J. Appl. Phys.*, 2005, **97**, 103706.

30 N. Wu, Y. Wu, D. Walter, H. Shen, T. Duong, D. Grant, C. Barugkin, X. Fu, J. Peng, T. White, K. Catchpole and K. Weber, *Energy Technol.*, 2017, **5**, 1827–1835.

31 Z. Wang, Q. Lin, F. P. Chmiel, N. Sakai, L. M. Herz and H. J. Snaith, *Nat. Energy*, 2017, **2**, 17135.

32 M. Saliba, M. Stolterfoht, C. M. Wolff, D. Neher and A. Abate, *Joule*, 2018, **2**, 1019–1024.

33 Y. Zhang, F. Wu, L. Chen, F. Zhang, Y. Ji, W. Shen, M. Li, Q. Guo, W. Su and R. He, *Sol. Energy Mater. Sol. Cells*, 2020, **212**, 110534.

34 S. Valero, S. Collavini, S. F. Völker, M. Saliba, W. R. Tress, S. M. Zakeeruddin, M. Grätzel and J. L. Delgado, *Macromolecules*, 2019, **52**, 2243–2254.

35 Z. Hawash, L. K. Ono and Y. Qi, *Adv. Mater. Interfaces*, 2016, **3**, 1600117.

36 J. Xia, R. Zhang, J. Luo, H. Yang, H. Shu, H. A. Malik, Z. Wan, Y. Shi, K. Han, R. Wang, X. Yao and C. Jia, *Nano Energy*, 2021, **85**, 106018.

37 S. Wang, M. Sina, P. Parikh, T. Uekert, B. Shahbazian, A. Devaraj and Y. S. Meng, *Nano Lett.*, 2016, **16**, 5594–5600.

38 E. J. Juarez-Perez, M. R. Leyden, S. Wang, L. K. Ono, Z. Hawash and Y. Qi, *Chem. Mater.*, 2016, **28**, 5702–5709.

39 C. Ahläng, M. Nyman and R. Österbacka, *Phys. Rev. Appl.*, 2021, **16**, 014041.

40 V. M. Le Corre, M. Stolterfoht, L. Perdigón Toro, M. Feuerstein, C. Wolff, L. Gil-Escrig, H. J. Bolink, D. Neher and L. J. A. Koster, *ACS Appl. Energy Mater.*, 2019, **2**, 6280–6287.

41 A. Kaliszewska, J. Allison, M. Martini and N. Arias, *Int. J. Mol. Sci.*, 2021, **22**, 3574.

42 J. Euvrard, A. Revaux, P. A. Bayle, M. Bardet, D. Vuillaume and A. Kahn, *Org. Electron.*, 2018, **53**, 135–140.

This journal is © The Royal Society of Chemistry 2022

J. Mater. Chem. A, 2022, **10**, 11721–11731 | 11731